

Enhancing State Estimator for Autonomous Race Car : Leveraging Multi-modal System and Managing Computing Resources

Daegy Lee¹, Hyunwoo Nam², Chanhoe Ryu¹, Sungwon Nah², Seongwoo Moon¹ and D. Hyunchul Shim^{1*}

Abstract—This paper introduces an innovative approach to enhance the state estimator for high-speed autonomous race cars, addressing challenges related to unreliable measurements, localization failures, and computing resource management.

The proposed robust localization system utilizes a Bayesian-based probabilistic approach to evaluate multimodal measurements, ensuring the use of credible data for accurate and reliable localization, even in harsh racing conditions.

To tackle potential localization failures during intense racing, we present a resilient navigation system. This system enables the race car to continue track-following by leveraging direct perception information in planning and execution, ensuring continuous performance despite localization disruptions.

Efficient computing resource management is critical to avoid overload and system failure. We optimize computing resources using an efficient LiDAR-based state estimation method. Leveraging CUDA programming and GPU acceleration, we perform nearest points search and covariance computation efficiently, overcoming CPU bottlenecks.

Real-world and simulation tests validate the system’s performance and resilience. The proposed approach successfully recovers from failures, effectively preventing accidents and ensuring race car safety.

Index Terms—Navigation, Sensors, Multimodal Systems

I. INTRODUCTION

High-performance robotics racing is emerging as a powerful platform for driving development and showcasing state-of-the-art capabilities in autonomous systems. The first Indy Autonomous Challenge (IAC) started in October 2021, utilizing the Dallara IL-15 IAC race car, equipped with six mono-cameras, three radars, three LiDARs, and two real-time kinematic (RTK) GPS. Since then, four races have taken place, including two at the Consumer Electronics Show (CES) in Las Vegas, one in Texas in November 2022, and the most recent one in Monza, Italy. These competitions place a specific focus on advancing software that can handle edge cases in

¹ Department of Electrical Engineering, Korea Advanced Institute of Science and Technologies (KAIST), Daejeon, Republic of Korea {lee.dk, ryuchanhoe, seongwoo.moon, hcshim}@kaist.ac.kr

² Robotics Program, KAIST, Daejeon, Republic of Korea {menu107, sw.nah}@kaist.ac.kr

* Corresponding Author

This work was supported by the Technology Innovation Program (RS-2023-00256794, Development of drone-robot cooperative multimodal delivery technology for cargo with a maximum weight of 40kg in urban areas) funded by the Ministry of Trade, Industry & Energy(MOTIE, Korea).

This work has been submitted to the IEEE for possible publication. Copyright may be transferred without notice, after which this version may no longer be accessible.



Fig. 1. (a)Dallara AV-21 of Team KAIST at the Las Vegas Motor Speedway (LVMS) (b)IONIQ 5 of Team KAIST for HAC 2023.

autonomous driving, even in scenarios involving speeds of up to 300 kph.

Parallel to these developments, a new autonomous racing competition, known as the Hyundai Autonomous Challenge (HAC), is emerging in South Korea, featuring Hyundai Motors’ electric car, the IONIQ 5. While each team can customize the sensors for their vehicles, there is a common trend toward using LiDAR and GPS/INS in the high-speed navigation algorithm. The primary goal of this competition, like the IAC, is to stimulate the advancement of autonomous driving technology.

However, in deploying these high-speed race cars, it was found that the majority of accidents were caused by issues with the navigation systems. Consequently, all participating teams need to handle the unreliable sensor measurements, which negatively impacted localization performance. In particular, the GPS, despite being the most critical sensor for localization, presented significant challenges. During high-speed driving, strong vibrations often caused drifts in the GPS’s position solution, leading to serious accidents.

To overcome the aforementioned issues and achieve a higher level of system robustness, a more comprehensive approach to localization is required. This can be achieved through multimodal sensing, which involves utilizing multiple types of sensors to gather varied data. In this study, we employ GPS/INS and LiDARs as our main sensors. Leveraging this multimodal sensing system, we propose a resilient and efficient localization system as follows.

- Real-time identification of measurement reliability through a probabilistic Bayesian approach, enabling selective updates by filtering out unreliable measurements.
- An efficient LiDAR-based state estimation method, com-

posed of two main concepts: computing efficient scan matching for correction, and LiDAR odometry for prediction, both accelerated by CUDA.

- A resilient navigation system that utilizes direct LiDAR measurements to maintain safe operation of the system, even in the event of localization failures.

Throughout a series of computer simulations and experiments on real racetracks, it is validated that the proposed robust localization algorithm and the efficient navigation module are capable of maintaining high-speed racing even when all GPS sensors are temporarily deteriorated.

The remainder of the paper is organized as follows. Section II introduces related studies. Section III describes our high-speed, resilient state estimator leveraging GPS/INS and LiDAR. The experimental results, including simulated and real-world tests, are discussed in Section IV. Finally, Section V concludes this paper.

II. RELATED WORKS

A. Localization based on multi-sensor fusion

The key challenge of navigation is adapting, learning, and recovering from failures [1]. To address this issue, multi-sensor fusion has been studied. A challenge is to integrate multiple sensors and distinguish between accurate and unreliable ones. Tightly coupled navigation with global navigation satellite system (GNSS), LiDAR, inertial measurement unit (IMU) is proposed in [2], [3]. In addition, Soloviev *et al.* [4] presented tight coupling of LiDAR and IMU without GPS. However, these applications are deployed on the limited scenes due to 2D laser scanner. Recently, robust and precise localization system is proposed [5]. In the study, they evaluated the localization system in various city scenes by integrating 3-D LiDAR, GPS, and IMU. However, only one sensor of each type was used.

In most open sky environments, GPS plays an important role in localization by providing accurate global position, but their performance might be impacted in environments with occlusions, multi-path or radio interferences. Therefore, LiDAR-based multi-sensor fusion for GPS-denied environments are significantly studied [6]–[8]. In this study, we utilize GPS/INS and LiDAR for high-speed driving systems, and present research on multimodal measurement utilizing multiple GPS and LiDAR.

B. Perception based navigation system

Perception based navigation systems offer high accuracy and flexibility in dynamic environments, particularly by enabling continued navigation even in the absence of GPS signals. Wall following navigation based on LiDAR sensors has demonstrated promising results [9]–[11]. In these studies, a wall following algorithm was introduced for mobile platforms, primarily using 2D LiDAR sensors. However, our system employs 3D LiDAR, requiring ground filtering to distinguish between walls and the ground. Additionally, when applied to high-speed autonomous vehicles on a race track, wall following approach presents unique challenges.

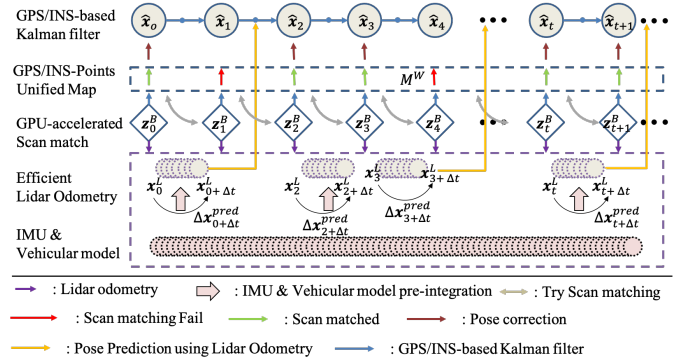


Fig. 2. State estimator for high-speed race car

RGB images can also be utilized for perception-based navigation system [12]. To improve image-based approach, hybrid methods that combine point-cloud and images have been proposed in recent studies [13], [14]. Recently, deep-perception-based approaches have been studied for autonomous race cars [15]–[19], but there are needs to ensure the output is reliable without fatal errors in real-world. Therefore, there are still limitations in deploying learning-based methods for real-world applications.

C. Autonomous racing

In the past few years, scale RC cars have been used to investigate algorithms for autonomous racing experimentally [20], [21]. A comprehensive overview of the current autonomous racing platforms, emphasizing the software-hardware co-evolution to the current stage, is presented in [22]. After a series of IAC races, each team presented its full stack of autonomous systems and approaches in [23]–[25]. Moreover, TUM Autonomous Motorsport team presented their planning and control modules [26]–[31]. In addition, when autonomous racing becomes analogous to human-driven racing competition, behavior planning would be one of the most important systems performing overtaking or decision-making. Hence, we studied the game-based predictor to predict future trajectories of racing competitors for overtaking or decision-making in autonomous racing [32].

III. METHODS

To integrate multimodal measurement system, our full state estimator is designed as shown in Fig. 2. We integrate a Kalman filter-based GPS/INS method with a LiDAR-aided state estimation algorithm.

A. Multimodal measurement fusion Kalman filter

For multimodal sensor fusion, we use an extended Kalman filter algorithm. Although Kalman filter enables us to combine information from multiple GPS units and LiDAR sensors, its performance deteriorates rapidly when unreliable measurements are fed to the filter. In order to prevent such situations, we identify measurement reliability in real-time through a

probabilistic Bayesian approach, and selectively update the multimodal measurements.

We propose our multimodal measurement fusion Kalman filter algorithm to deal with GPS measurement noise due to strong vibrations. To obtain global positioning using LiDAR, we create a pre-built map of a race track and apply a scan-matching algorithm.

1) *Vehicle state estimation formulation*: The Kalman filtering process of time-varying stochastic control system with k multiple measurements is given by

$$\begin{aligned}\mathbf{x}_t &= \mathbf{F}_{t-1}\mathbf{x}_{t-1} + \mathbf{B}_{t-1}\mathbf{u}_{t-1} + \mathbf{q}_t, \\ \mathbf{y}_t^k &= \mathbf{H}_{t-1}^k\mathbf{x}_{t-1} + \mathbf{v}_t,\end{aligned}\quad (1)$$

where $\mathbf{x}_t \in \mathbb{R}^n$ is the state, $\mathbf{y}_t^k \in \mathbb{R}^m$ is the k -th measurement, and $\mathbf{u}_t \in \mathbb{R}^l$ is the control input. $\mathbf{q}_t \sim \mathcal{N}(0, \mathbf{Q})$ and $\mathbf{v}_t \sim \mathcal{N}(0, \mathbf{R})$ are an additive white Gaussian noise (AWGN). Specifically, to achieve time-efficient state estimation with the available computation hardware, we used extended kalman filter (EKF) with constant turn rate and velocity (CTRV) model [33]. Therefore, we denote the vehicle state as

$$\begin{aligned}\mathbf{x}_t &= [x_t, y_t, \theta_t, b_t]^T, \\ \mathbf{u}_t &= [v_{x,t}, w_{z,t}]^T, \\ \mathbf{y}_t^k &= [\mathcal{Z}_{x,t}^k, \mathcal{Z}_{y,t}^k, \mathcal{Z}_{\theta,t}^k]^T,\end{aligned}\quad (2)$$

where $\{x_t, y_t, \theta_t\} \in SE(2)$ are vehicle's coordinate, heading, and b_t is yaw bias. Control input $\{v_{x,t}, w_{z,t}\}$ are longitudinal velocity and yaw velocity, respectively, and they are obtained from the vehicle electronics and IMU. We assume the evolution of each element in Eq. 2 is described by and vehicle's nonlinear kinematics model as

$$\begin{aligned}x_t &= x_{t-1} + v_{x,t-1}\cos(\theta_{t-1} + b_{t-1})dt, \\ &= x_{t-1} + \psi_{t-1}dt \\ y_t &= y_{t-1} + v_{x,t-1}\sin(\theta_{t-1} + b_{t-1})dt, \\ &= y_{t-1} + \phi_{t-1}dt \\ \theta_t &= \theta_{t-1} + w_{z,t-1}dt, \\ b_t &= b_{t-1}, v_{x,t} = v_{x,t-1}, w_{z,t} = w_{z,t-1}.\end{aligned}\quad (3)$$

To extend linear model with Eq. 1, we obtain the discrete-time evolution model with time-dependent linearized matrix \mathbf{A}_t as

$$\mathbf{x}_t = \mathbf{A}_t \cdot \mathbf{x}_{t-1} + \mathbf{q}_t, \quad (4)$$

where \mathbf{A}_t can be represented as

$$\mathbf{A}_t = \begin{bmatrix} 1 & 0 & \dot{\psi}_{t-1} \cdot dt & \dot{\phi}_{t-1} \cdot dt & \psi_{t-1}/v_{x,t-1} \cdot dt & 0 \\ 0 & 1 & \dot{\phi}_{t-1} \cdot dt & \dot{\psi}_{t-1} \cdot dt & \phi_{t-1}/v_{x,t-1} \cdot dt & 0 \\ 0 & 0 & 1 & 0 & 0 & dt \\ 0 & 0 & 0 & 1 & 0 & 0 \\ 0 & 0 & 0 & 0 & 1 & dt \\ 0 & 0 & 0 & 0 & 0 & 1 \end{bmatrix}. \quad (5)$$

2) *Problem definition*: Our goal is to estimate vehicle state with k observation model to obtain the k observations vector as

$$\mathbf{y}_t^k = \mathbf{h}^k(\mathbf{x}_t) + \mathbf{v}_t. \quad (6)$$

We can address our localization problem as the posterior probability in terms of the prior likelihood [34]. Our problem definition starts with optimizing the overall state of $\hat{\mathbf{x}}_t$ with multiple observations \mathbf{y}_t^k :

$$\{\hat{\mathbf{x}}_t\}_{t \in [1,t]} = \arg \max_{\mathbf{x}_t} \left[\prod_{i=0}^t p(\mathbf{x}_i | \mathbf{x}_{i-1}) p(\mathbf{y}_i^k | \mathbf{x}_i) p(\mathbf{y}_0^k | \mathbf{x}_0) p(\mathbf{x}_0) \right]. \quad (7)$$

We define our localization problem as finding an optimal solution at the current time t ; a marginalization can be represented as follows:

$$\begin{aligned}\hat{\mathbf{x}}_t &= \arg \max_{\mathbf{x}_t} \left[\int p(\mathbf{y}_t^k | \mathbf{x}_t) p(\mathbf{x}_t | \mathbf{x}_{t-1}) \right. \\ &\quad \left. \prod_{i=0}^t p(\mathbf{x}_i | \mathbf{x}_{i-1}) p(\mathbf{y}_i^k | \mathbf{x}_i) p(\mathbf{y}_0^k | \mathbf{x}_0) p(\mathbf{x}_0) d\{\mathbf{x}_l\}_{l \in [1,t-1]} \right],\end{aligned}\quad (8)$$

where we assume each variable as independent and identically distributed. We further simplify Eq. 8 as

$$\hat{\mathbf{x}}_t \propto \arg \max_{\mathbf{x}_t} \left[\int p(\mathbf{y}_t^k | \mathbf{x}_t) p(\mathbf{x}_t | \mathbf{x}_{t-1}) d\{\mathbf{x}_l\}_{l \in [1,t-1]} \right]. \quad (9)$$

Using Bayes' theorem, we propose a hyper-parameter Θ for localization to conditionally update the measurement as follows:

$$\hat{\mathbf{x}}_t \propto \arg \max_{\Theta} \left[\int p(\mathbf{y}_t^k | \Theta^k) p(\Theta^k | \mathbf{x}_t) p(\mathbf{x}_t | \mathbf{x}_{t-1}) d\{\mathbf{x}_l\}_{l \in [1,t-1]} \right]. \quad (10)$$

Intuitively, it is the likelihood of the k -th measurement \mathbf{y}_t^k over all possible parameter values, weighted by the prior $p(\Theta^k | \mathbf{x}_t)$. If all localization hyper-parameter $p(\Theta^k)$ assign high probability to the k -th measurement data, then this is a reasonable criterion for multiple measurements. We define our multimodal measurement fusion algorithm for high-speed localization as finding $p(\mathbf{y}_t^k | \Theta^k)$ and $p(\Theta^k | \mathbf{x}_t)$. Therefore, we determine a poor signal quality computing hyper-parameter Θ to prevent using weak measurements to correct the Kalman filter. Our proposed Kalman filter for multimodal measurement and degradation identification is described in Fig. 3.

3) *Bayesian-based multimodal measurement update*: At a correction step of the Kalman filter, we propose a degradation identification method with a novel hyper-parameter $p(\Theta^k)$ derived from Bayesian decision theory. We assume $p(\Theta^k | \mathbf{x}_t)$ using the Mahalanobis distance Δ_k [35] as follows:

$$p(\Theta^k | \mathbf{x}_t) \triangleq 1 - 1/(1 + \exp(-\Delta_k)), \quad (11)$$

where Δ_k pass through the sigmoid function. Specifically, Δ_k can be obtained as

$$\Delta_k = (\mathbf{x}_{t-1} - \mathbf{y}^k)^T \Sigma_k^{-1} (\mathbf{x}_{t-1} - \mathbf{y}^k), \quad (12)$$

where \mathbf{y}^k is the k -th measurement and $\Sigma_k^{-1} = \Lambda_k$ is the k -th measurement precision matrix. Σ_k is updated with AWGN

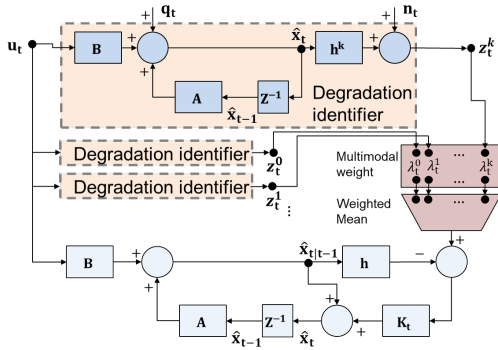


Fig. 3. Diagram of Kalman filter for multimodal measurement and degradation identification

\mathbf{v}_t and covariance value from measurement. More precisely, We interpret Δ_k as a Euclidean distance in an orthogonally transformed new coordinate frame to identify whether \mathbf{y}^k is a reasonable input or not.

We propose a novel method for updating measurements, which is based on Bayesian decision theory. Let $p(\mathbf{y}_i^k | \Theta^k, \mathbf{x}_i)$ defined conditional to Δ_k as follows:

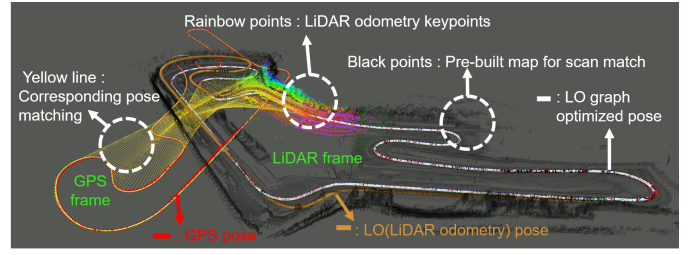
$$p(\mathbf{y}_i^k | \Theta^k, \mathbf{x}_i) = \begin{cases} \mathbf{y}^0 & \text{if } \forall \Delta_k \leq \epsilon \\ \lambda_i \cdot \mathbf{y}^i & \text{if } \forall \Delta_k > \epsilon \text{ and } \forall \Delta_k \leq \delta \\ \mathbf{y}^k & \text{if } \Delta_k \leq \delta \text{ and } \forall \Delta_{\sim k} > \delta \\ \lambda_{reject} & \text{if } \forall \Delta_k > \delta, \end{cases} \quad (13)$$

where $\lambda_k = 1 - \Delta_k / \sum(\Delta_i)$, δ , and ϵ are the measurement update weight, hyper-parameter to determine qualified measurement, and error ($\epsilon \ll \delta$), respectively. If all Δ_k is less than ϵ , we use one of the measurements because it is already qualified. If all Δ_k is less than δ , we implement the weighted sum of measurement, assuming that all the measurement is in reasonable condition. In contrast, if Δ_k is less than δ , but $\Delta_{\sim k}$ is greater than δ , we use the only one feasible measurement \mathbf{y}^k . Here, $\sim k$ in $\Delta_{\sim k}$ denotes complement set of Δ_k . Lastly, if all the distance is unsuitable for measurement updates, a warning alarm is raised to be ready for the resilient localization system to be discussed in the next section III-D. If the new measurement status is rejected, we update our state only depending on control input \mathbf{u}_t and not utilizing \mathbf{y}^k at all.

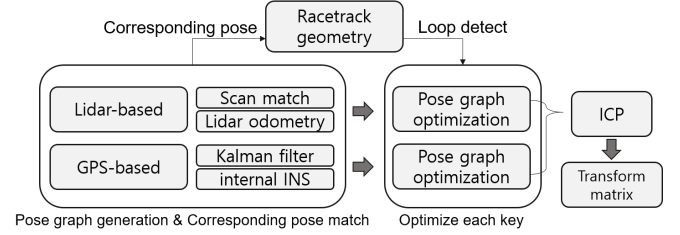
B. Unified frame map generation

In a multi-modal system, establishing accurate transformations between multiple global frames is crucial, as depicted in fig. 4(a). To effectively utilize a LiDAR scan-matched pose $\mathbf{y}_{scan}^k \in \mathbf{y}^k$ as a multimodal measurement, generating a unified map based on GPS frames is more intuitive, given that \mathbf{y}_{scan}^k can be directly integrated.

To facilitate this process, we utilize pose-graph optimization, designed to construct a unified 3-D map denoted as \mathbf{M}^W . This is achieved by minimizing the spatial separation between corresponding poses within the map. Importantly, the section introduces a unique pose-graph optimization-based



(a)



(b)

Fig. 4. The corresponding pose graph is visualized, showcasing the relationship between the LiDAR point cloud and GPS/INS frames of National Automobile Racetrack of Monza, Italy.

frame unification method tailored specifically for the racetrack environment. The outlined approach is depicted in fig. 4(b).

Using GTSAM framework [36], we update factor graphs using the GPS/INS key pose $\mathbf{x}_i^G \in \mathbf{x}_i$ and LiDAR key pose $\mathbf{x}_i^L \in \mathbf{x}_i$. Therefore, the factor graphs can be represented as

$$\begin{aligned} f_0(\mathcal{X}_0^G, \mathbf{x}_1^G, \dots, \mathbf{x}_{n-1}^G) &= \prod f_i(\mathcal{X}_i^G), \\ f_0(\mathcal{X}_0^L, \mathbf{x}_1^L, \dots, \mathbf{x}_{n-1}^L) &= \prod f_i(\mathcal{X}_i^L), \end{aligned} \quad (14)$$

where f_i indicates the connectivity of a factor graph's each factor.

To update the GPS/INS-based pose graph $f_i(\mathcal{X}_i^G)$ and LiDAR-based pose graph $f_i(\mathcal{X}_i^L)$, we process each frame individually. The update equations for GPS/INS-based odometry measurements are:

$$\begin{aligned} f_0(\mathcal{X}_0^G) &= f_0(\mathbf{x}_1^G), & \text{for } i = 0 \\ f_i(\mathcal{X}_i^G) &= f_i(\mathbf{x}_i^G, \mathbf{x}_{i+1}^G; \mathbf{o}_i^G), & \text{for } i > 0 \end{aligned} \quad (15)$$

For LiDAR odometry measurements:

$$\begin{aligned} f_0(\mathcal{X}_0^L) &= f_0(\mathbf{x}_1^L), & \text{for } i = 0 \\ f_i(\mathcal{X}_i^L) &= f_i(\mathbf{x}_i^L, \mathbf{x}_{i+1}^L; \mathbf{o}_i^L), & \text{for } i > 0 \end{aligned} \quad (16)$$

Here, \mathbf{o}_i^G represents GPS/INS-based odometry measurements, and \mathbf{o}_i^L represents LiDAR odometry measurements. For $i = 0$, the initial pose is updated using unary factors $f_0(\mathbf{x}_1^G)$ and $f_0(\mathbf{x}_1^L)$ for GPS/INS and LiDAR respectively. For subsequent poses ($i > 0$), the updates depend on factors $f_i(\mathbf{x}_i^G, \mathbf{x}_{i+1}^G; \mathbf{o}_i^G)$ and $f_i(\mathbf{x}_i^L, \mathbf{x}_{i+1}^L; \mathbf{o}_i^L)$ for GPS/INS and LiDAR respectively.

By using the GPS/INS-based pose as our main frame, our idea is to utilize racing line waypoints, as race tracks are typically loop-shaped. Therefore, we propose a hash-based

racetrack ID matching algorithm to associate a racetrack ID with GPS pose keys and corresponding LiDAR pose keys. For each GPS/INS pose key \mathbf{x}_i^G and corresponding LiDAR pose key \mathbf{x}_i^L :

$$\text{racetrack_dict}[\mathbf{x}_i^G, \mathbf{x}_i^L] \rightarrow \text{racetrack_geometric_id}$$

After successfully finding a loop closing pose from corresponding *racetrack_geometric_id*, we update the GPS/INS-based and LiDAR-based pose factors as follows:

$$\begin{aligned} f_i(\mathcal{X}_i^G) &= f_i(\mathbf{x}_i^G, \mathbf{x}_{\text{loop}}^G; \mathbf{o}_{\text{loop}}^G), \\ f_i(\mathcal{X}_i^L) &= f_i(\mathbf{x}_i^L, \mathbf{x}_{\text{loop}}^L; \mathbf{o}_{\text{loop}}^L), \end{aligned} \quad (17)$$

After conducting several iterative drives on the race course, we perform non-linear graph optimization using incremental smoothing and mapping (iSAM)-based optimization [?]. Subsequently, we run an iterative closest point (ICP) algorithm between the graphs to find a transformation matrix that aligns them. The transformation matrix is then used to generate a unified map, integrating the information from both GPS/INS-based and LiDAR-based pose graphs.

C. Efficient LiDAR-based state estimator

1) *Efficient registration method*: CPU-based registration may encounter bottlenecks due to its sequential nature. More precisely, finding corresponding points and computing covariance for relevant points can be computationally expensive, leading to slower performance, particularly with large and complex point clouds.

By adopting GPU-based methods, we can overcome these bottlenecks and achieve faster and more scalable point cloud registration. By implementing a GPU-based nearest points search and covariance computation using the kernel descriptors, we can leverage parallel processing capabilities to significantly accelerate the registration algorithm. GPU computation is ideal for handling large-scale point cloud data, enabling efficient computations on multiple points simultaneously.

We consider several kernel descriptors, each with its corresponding equation, to measure similarity between data points. The Radial basis function (RBF) kernel (K_{rbf}) [37], The Gaussian kernel (K_{gauss}), the Polynomial kernel (K_{poly}), the Histogram Intersection kernel (HI) (K_{hist}), and the Laplacian kernel ($K_{\text{laplacian}}$) are presented in Table I. In this study, the Laplacian method demonstrates the best performance among the considered kernel descriptors in GPU-based registration methods. Our implementation extends and optimizes the Voxelized-GICP algorithms, leading to superior results.

2) *LiDAR-inertial-vehicle model odometry for prediction*: By utilizing LiDAR odometry predictions for the initial transformation, we aim to enhance the convergence and accuracy of the ICP-variant algorithm during scan matching. This predictive approach leverages the motion estimation from LiDAR data, providing a more informed starting point for the iterative scan matching process.

To tackle the challenges posed by high-speed scenarios, we present an efficient LiDAR-inertial-vehicle model odometry algorithm. This algorithm leverages LiDAR data to predict the

TABLE I
KERNEL DESCRIPTOR

Kernel Descriptor	Equation
RBF	$K_{\text{rbf}}(x, y) = \exp(-\ x - y\ ^2 * \sigma)$
Gaussian	$K_{\text{gauss}}(x, y) = \exp\left(-\frac{\ x - y\ ^2}{2\sigma^2}\right)$
Polynomial	$K_{\text{poly}}(x, y) = (\alpha(x, y) + c)^d$
HI	$K_{\text{hist}}(x, y) = \frac{\sum \min(x^{[i]}, y^{[i]})}{\sum x^{[i]}}$
Laplacian	$K_{\text{laplacian}}(x, y) = \exp\left(-\frac{\ x - y\ }{\sigma}\right)$

vehicle's pose accurately. By incorporating the inertial information and the vehicle model, we can efficiently estimate the pose of the vehicle, enabling precise and real-time predictions in high-speed driving situations.

Firstly, we incorporate inertial data, specifically the rotational velocity \mathbf{w}_t . For rotational pose prediction, we use the quaternion \mathbf{q}_t obtained from the IMU pre-integrator. We predict the rotation matrix for the next time step as:

$$\mathbf{q}_{t+1} = \mathbf{q}_t + \left(\frac{1}{2}\mathbf{q}_t \otimes \mathbf{w}_t\right) \Delta t, \quad (18)$$

where Δt operator makes time difference between consecutive scan data. This prediction is based on quaternion multiplication \otimes , where the quaternion \mathbf{q}_t is updated using the rotational velocity \mathbf{w}_t . This approach allows us to estimate the rotational component of the pose even in the absence of direct inertial measurements.

To address the noise inherent in the inertial sensor's acceleration measurements, we utilize a vehicle model for the linear velocity-based pose preintegration. The translational component of the pose is predicted using the translation vector \mathbf{t}_t obtained from the vehicle model pre-integrator, considering the rotation pre-integrator from the IMU. The prediction is computed as:

$$\mathbf{t}_{t+1} = \mathbf{t}_t + \left(\mathbf{q}_t \otimes \begin{bmatrix} v_x \Delta t \\ v_y \Delta t \\ 0 \end{bmatrix} \otimes \mathbf{q}_{\theta_t}^{-1}\right), \quad (19)$$

where \mathbf{t}_t is the translational component of the pose at time step t and $[v_x \Delta t, v_y \Delta t, 0]^T$ represents the displacement. $\mathbf{q}_{\theta_{t+1}}^{-1}$ represents the quaternion representing the inverse of the rotation due to the steering angle θ_{t+1} . We first rotate the displacement due to linear velocity $[v_x \Delta t, v_y \Delta t, 0]^T$ by \mathbf{q}_t to account for the vehicle's current orientation. Then, we further rotate the result by $\mathbf{q}_{\theta_t}^{-1}$ to incorporate the effect of the steering angle θ_t and the vehicle's kinematic model correctly.

We consider LiDAR odometry's next scan match initial guess $\mathbf{x}_{t+1}^{\dagger L}$ as :

$$\mathbf{x}_{t+1}^{\dagger L} = \mathbf{x}_t^L * \begin{bmatrix} \Delta \mathbf{q}_t & \Delta \mathbf{t}_t \\ 0 & 1 \end{bmatrix}. \quad (20)$$

With inertial and vehicular model data, we could obtain a more accurate pose estimation results.

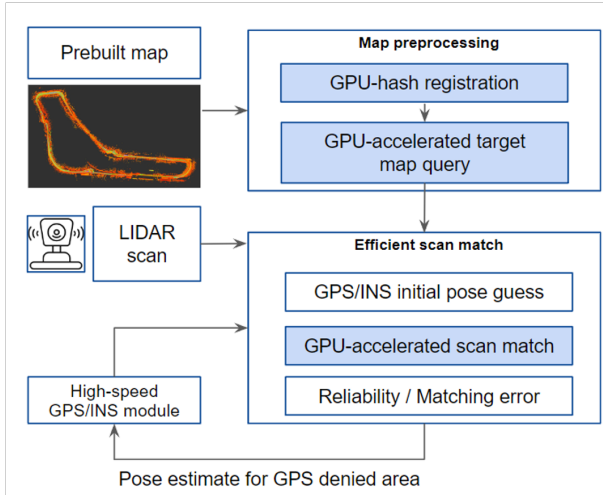


Fig. 5. Proposed pipeline of GPU-accelerated scan match algorithm

3) *Scan match for correction:* Utilizing a unified frame map, we can leverage the scan match pose $\mathbf{y}_{scan}^k \in \mathbf{y}^k$ as a multimodal measurement. To achieve efficient point cloud registration, we have implemented the optimized registration algorithm discussed in section III-C1. Nonetheless, for optimal performance in high-speed driving scenarios, the development of a finely-tuned scan-matching algorithm remains crucial.

The key idea is an efficient target map query process of the point cloud map \mathbf{M}^W using a GPU-hash data structure. This process is vital, especially for large race tracks. By leveraging the GPU-hash data structure, we associate each pose on the race line with its corresponding point cloud map [37].

In pursuit of efficiency, we employ a sliding-window approach by utilizing points from $\mathbf{M}_i^\psi \subset \mathbf{M}^W$ [7], [38] instead of processing the entire unified map \mathbf{M}^W . This sliding-window strategy contributes to the overall efficiency of the pipeline, especially when iteratively extracting a smaller window sliding map from the larger map. Furthermore, the performance of the ICP-variant algorithm is improved by considering predictive transformations of scan query data using LiDAR odometry predictions. This approach leverages LiDAR motion estimation to enhance the algorithm’s convergence and accuracy during scan matching, resulting in more efficient and precise results.

Lastly, in the event of scan matching failure and when reliability exceeds predetermined safety thresholds, our system incorporates a resilient GPS/INS module for swift recovery. A visual representation of our proposed pipeline is illustrated in Fig. 5.

D. Wall detection for resilient navigation

Since even the proposed robust localization system temporarily fails due to harsh conditions on the racetrack, we propose additional wall-following navigation module which does not depend on the main localization system. It provides extended resilience to the navigation system as it produces safe lateral control at the moment of a complete localization

system malfunction due to multiple GPS failures. To detect the walls of the racetrack at extreme driving speeds, we propose an efficient ground filtering algorithm that only uses direct LiDAR measurements.

When our proposed multimodal measurement fusion Kalman filter keeps computing $p(\mathbf{y}_i^k | \Theta^k, \mathbf{x}_i)$ as λ_{reject} , we consider this status as positioning degraded situation. To deal with these critical situations, we have designed our race car such that it follows along the race track wall, thereby avoiding collision with the wall. To extract a wall in the racing track, we propose a wall detection algorithm comprising of fast ground removal and wall clustering algorithms. The algorithm helps navigate the wall resiliently when a deterioration is detected in the entire measurement.

1) Vertical feature extraction for fast ground filtering:

Generally, the race track is mostly banked road, which angles towards the race track center to help vehicles speed up at curved corners. Thus, the ground filtering algorithm for LiDAR points has to consider the road gradient.

We propose a novel vertical feature extractor using a hashing algorithm to consider the sparsity of LiDAR point-cloud data. Let $B \subset \mathbb{R}^3$ define the vehicle body coordinates. Here, B annotated values indicating the information obtained from the vehicle body’s origin—i.e., the center point of the rear axle. We also define the voxel-filtered LiDAR points $\mathbf{p}_t^B = \{p_1^B, \dots, p_k^B\}$ at time t , where p_i^B is a voxelized point from the incoming LiDAR points. After voxelization, we project \mathbf{p}_t^B to the 2-D grid to vote the points corresponding to the grid-cell, as shown in Fig. 6(a). Moreover, we propose a hashing algorithm during the voting to account for the sparsity of the point cloud.

$$\begin{aligned} H(p_i^B) &= index, \\ H^{-1}(index) &= p_i^B, \end{aligned} \quad (21)$$

where hash function $H(x)$ maps the value x at the table. We iterate voxelized points \mathbf{p}_t^B to vote on the corresponding grid-cell using $f(p_i^B) = g(u_i, v_i, \mathbf{n}_{index})$ where \mathbf{n}_{index} contains the number of points voted and its hashing-index. Thus, by comparing \mathbf{n}_{index} size with hyper-parameter, we can efficiently filter out ground points \mathbf{p}_t^{ground} from \mathbf{p}_t^B in real-time without matrix computation for plane extraction.

2) *Wall following navigation:* To extract the plane feature from the point-cloud, we implement a random sample consensus (RANSAC)-variant algorithm [39], [40]. However, a distance parameter determines the inlier or outlier points, which is unsuitable for curved wall areas. Our approach uses a common tree-based Euclidean distance algorithm to find a wall from the ground-filtered points $\mathbf{p}_t^{filtered}$, as shown in Fig. 6(c). We implement a CUDA-based Euclidean distance clustering algorithm [41], [42] to find cluster C_j [43]:

$$\begin{aligned} C_j &= \arg \min_i \| p_i^{filtered} - \mu_j \|_2, \\ \mu_j &= \frac{\sum_{i=1}^m \mathbf{1}\{c^i = j\} p_i^{filtered}}{\sum_{i=1}^m \mathbf{1}\{c^i = j\}}, \end{aligned} \quad (22)$$

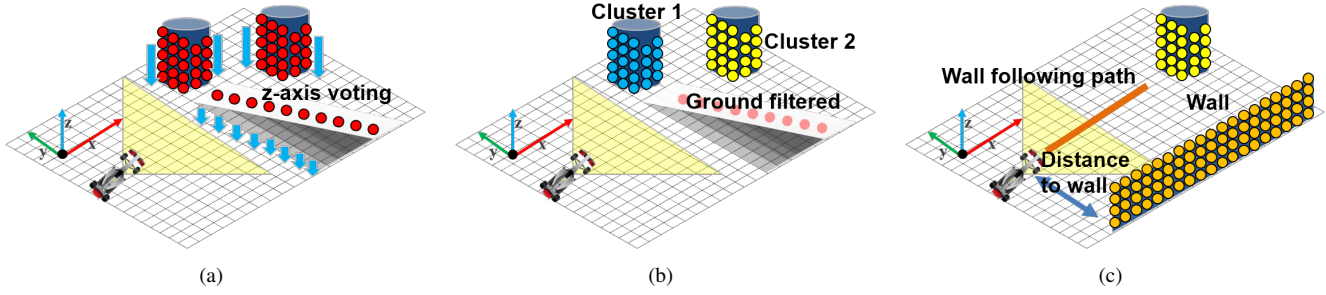


Fig. 6. Description of process for ground points filtering, clustering, and wall detection. (a) Ground filtering based on a z-axis voting algorithm. The number of voting to grid-cell is compared to a hyper-parameter to extract the vertical features. In the illustration, points corresponding to the banked road have a few counts. (b) Ground-filtered points are illustrated. In addition, the Euclidean-distance clustering algorithm is implemented. (c) The length of clusters is used, assuming that the longest right-side cluster is the wall. Points of the wall are computed to estimate the wall curvature and distance to the wall.

where Eq. 22 is the subject condition for clustering algorithm. We assume the longest cluster as wall cluster $\mathbf{w}_i(x_{w,i}, y_{w,i})$:

$$\mathbf{w}_i(x, y) = \mathbf{P}_z \cdot \arg \max_x (\mathcal{H}(C_j(x_{w,i}, y_{w,i}, z_{w,i}))), \quad (23)$$

where $\mathcal{H}(x)$ extracts the length of clusters, and \mathbf{P}_z is the z-directional projection matrix.

We then obtain a coefficient of the polynomial regression model $\hat{\beta}_w$ of $\mathbf{w}_i(x_{w,i}, y_{w,i})$ as follows:

$$\hat{\beta}_w = (\mathbf{X}_w^T \mathbf{X}_w)^{-1} \mathbf{X}_w^T \mathbf{y}_w, \quad (24)$$

where $\mathbf{X}_w = \{x_{w,i} \in \mathbf{w}_i(x_{w,i}, y_{w,i})\}_{i=1:n}$ and $\mathbf{y}_w = \{y_{w,i} \in \mathbf{w}_i(x_{w,i}, y_{w,i})\}_{i=1:n}$. We next estimate the distance to the wall used for collision warning as follows:

$$d_w = \mathbf{y}_w(x_{w,0}), \quad (25)$$

where $x_{w,0}$ denotes the origin point on body coordinates of the vehicle's x-directional axis. Thus, we can calculate the desired lateral shift from the current position, $d_w - d_{gap}$, where d_{gap} denotes the desired distance from wall. Subsequently, we are able to generate a wall following path \mathbf{p}_w that maintains a desired distance from the wall as

$$\mathbf{p}_w(x_{w,i}) = \hat{\beta}_2 x_{w,i}^2 + \hat{\beta}_1 x_{w,i} + (d_w - d_{gap}), \quad (26)$$

where $\{\hat{\beta}_1, \hat{\beta}_2\} \subset \hat{\beta}_w$. The path is generated using the second-order polynomial curve fitting to address the characteristics of oval tracks. Afterwards, the generated path is being handled by the existing controller to track the given path accordingly. More details about the controller can be found in our other study [44].

IV. RESULTS

A. Test scenarios

During our evaluation, we conducted tests at speeds of up to 248.8 kph across four different race events held in different countries. The maximum speeds achieved for each event are detailed in Table II.

The US tracks, including Lucas Oil Raceway, Indianapolis Motor Speedway, Las Vegas Motor Speedway, and Texas Motor Speedway, provided a suitable environment to test high-speed scenarios. On the other hand, the Monza Circuit in

Italy and Everland Speedway in South Korea offered more dynamic scenarios with challenging corners such as hairpin turns and chicanes. These dynamic features posed significant challenges for state estimation, especially in dealing with lateral derivatives and dynamic rotational driving.

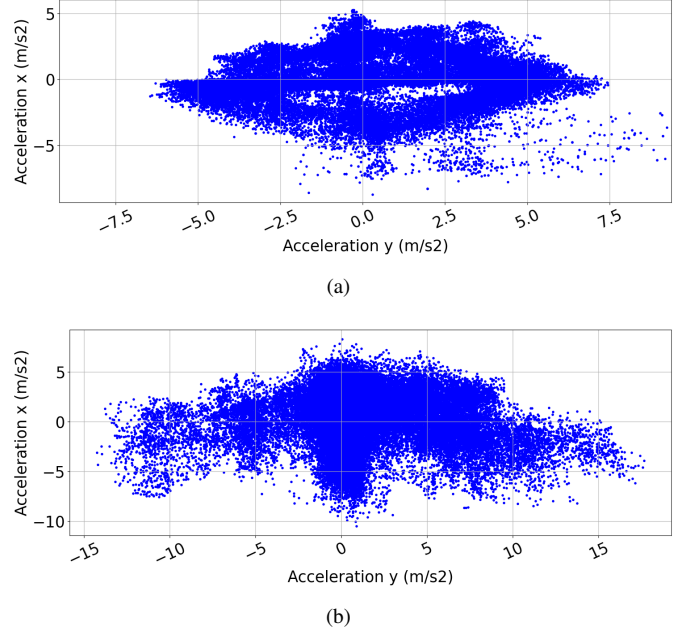


Fig. 7. GG-diagram illustrating different test scenarios: (a) GG-diagram of Everland Speedway, driven by Hyundai IONIQ 5. (b) GG-diagram of Monza Circuit, driven by Dallara Indy Lights car.

Figure 7 illustrates the gg-diagram of the Monza and Everland circuits, providing further insights into the test scenarios.

B. Vehicle platform

1) *Indy autonomous challenge*: The race car was based on a Dallara Indy Lights IL-15 chassis. The computation hardware was equipped with an ADLink x64 computer system based on an Intel Xeon with eight physical CPU cores and an NVIDIA RTX 8000 GPU. The sensor unit has two independent

TABLE II
FIELD TESTS PERFORMANCE SUMMARY.

Track	LOR	IMS	LVMS	TMS	MC	ES
Maximum speed	27.74 (m/s) 99.9 (km/h)	41.08 147.9	69.11 248.8	57.55 205.4	-	-

LOR : Lucas Oil Raceway, US **IMS** : Indianapolis Motor Speedway, US
LVMS : Las Vegas Motor Speedway, US **TMS** : Texas Motor Speedway, US
MC : Monza Circuit, Italy **ES** : Everland Speedway, South Korea

TABLE III
COMPUTING AND NETWORKING HARDWARE SPECIFICATIONS

Device	Specification
CPU	Intel Xeon E 2278 GE – 3.30 GHz (16T, 8C)
GPU	Nvidia Quadro RTX 8000 x 1 (PCIe slot)
RAM	64 GB
Ethernet ports	3 x GigE RJ45 (In-built) + 2 x 40GbE QSFP+ (PCIe-based)
CAN ports	4 x In-built ports, 2 x port on PCIe card
Network switch	Cisco IE-5000-12s12p-10G – 12 GigE copper 12 GigE fiber, 4x 10G uplink, PTP GM Clock
Wireless	Cisco/Fluidmesh FM4500 - up to 500Mbps
GPS	2 x NovAtel PwrPak7 + HxGN SmartNet RTK
LiDAR	3 x Luminar Hydra 120°
RGB camera	6 x optical camera
Radar	3 x Delphi(1 x ESR + 2 x MRR)

NovAtel PwrPak7-Ds, with a full multi-frequency integrating GNSS engine and embedded micro-electro-mechanical system (MEMS) IMU, three Luminar LIDAR, three Aptiv radar, and six Allied Vision cameras. In addition, vehicle states, such as wheel speeds and brake pressures, are available. More detailed information is represented in Table III.

2) *Hyundai Autonomous Challenge*: For the Hyundai competition, the race car was built on an Intel Xeon-based computation hardware with an NVIDIA GeForce RTX 3080 GPU. The vehicle was equipped with an array of sensors, including the Ouster OS2-128 LiDAR and two Velodyne VLP 16 puck LiDAR sensors mounted on the side parts. Additionally, the car featured four GMSL Seconix cameras for visual perception, while the GPS system consisted of a Ublox F9P receiver and a Microstrain GQ7 IMU for localization.

Detailed specifications of the computation and sensor hardware used in the Hyundai competition are provided in Table IV.

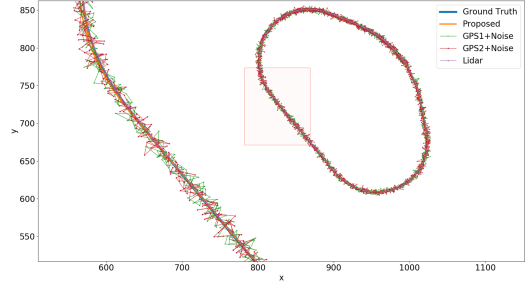
C. Multimodal measurement fusion Kalman filter

1) *Resilience to simulated error and noise*: We performed simulated tests to evaluate the capability of the proposed algorithm. We added significant artificial noise to the logged multimodal data, which included measurements from two GPS and one LiDAR sensors, with standard deviation noise of 5m and 10m as shown in Fig. 8(a).

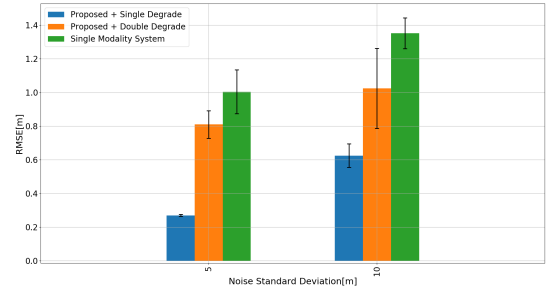
During the evaluation scenario, the vehicle averaged 225kph and reached 244kph at maximum speed. We compared the estimated pose error with the ground truth under conditions where one or two of the multimodal measurements were degraded, as well as in a single-modality system under identical conditions. When compared to a system based on a single

TABLE IV
HYUNDAI COMPETITION’S COMPUTING AND SENSOR HARDWARE SPECIFICATIONS

Device	Specification
CPU	Intel Xeon E - GHz (TBD)
GPU	Nvidia GeForce RTX 3080 (PCIe slot)
RAM	64GB
Ethernet ports	PCIe-PoE550X 2-port 10GbE
CAN ports	PEAK CAN on PCIe card
Network switch	Tp-link TL-SX1008-10G
Wireless	KT LTE Egg - up to 500Mbps
GPS	Ublox F9P + Microstrain GQ7
LiDAR	Ouster OS2-128 + 2 x Velodyne VLP 16
RGB camera	4 x GMSL Seconix camera



(a)



(b)

Fig. 8. Large-noise was artificially added to the multimodal measurements and the single modality system. (a) A simulated error on the LVMS race track. The degradation of both GPS is represented in magnified view. (b) Proposed algorithm successfully estimates the position robustly, compared to single modality system. Specifically, the accuracy performance was maintained even when one of the two degradation occurred.

modality, the proposed algorithm successfully estimates the position robustly. Specifically, the accuracy performance was maintained even when one of the two degradation occurred as depicted in Fig. 8(b).

2) *real-world test*: Regarding the specifics of implementation, we set ϵ as 0.2 m and δ as 5.0 m in Eq. 13. Figures 9(a)-9(d) present the magnified view of GPS and estimation data from the first day of the competition in IMS. Specifically, on the first competition day, we experienced more difficulties with faulty GPS antennas and heavy vibration, leading to a degradation of GPS performance. As depicted in Fig. 9(e), errors from two GPS units are shown during 20km driving. Despite frequent degradation, we were able to effectively reject

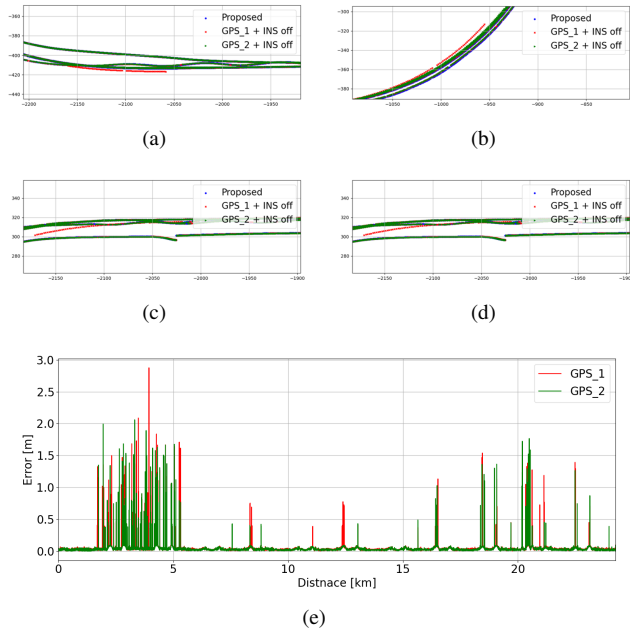


Fig. 9. Result of GPS log data and its estimated position using the proposed localization at IMS. Despite the degradation, the proposed localization algorithm estimated position resiliently throughout the track. (a)-(d) A magnified representation of the track is shown with partial degradation of the GPS data and an estimated result. (e) Errors from two GPS units are shown during 20km driving. Initially, the GPS signal deteriorated frequently, and corner sections drifted frequently. Ground-truth is manually generated to compute error.

degraded measurements through the methods proposed.

The operation of the tight INS/GNSS integration mode in the presence of heavy vibrations resulted in significant positioning degradation, particularly in the earlier IAC competitions. However, with the advancements in technology and the implementation of mechanical damping systems to mitigate vibrations, this issue has been gradually addressed and is now less prevalent in recent competitions.

Figure 9(e) shows the data from the first IAC competition in Indianapolis, illustrating the impact of vibrations on positioning accuracy.

D. Unified frame map generation

We evaluate the integrated robust state estimator, combining GPS/INS and efficient LiDAR-based state estimators, to assess its performance in high-speed and dynamic driving scenarios on the race track. Our evaluation aimed to validate the state estimator’s accuracy and reliability under challenging conditions.

Additionally, we introduced simulated LiDAR point cloud noise to create scenarios where the scan matching algorithm might fail during the drive. This allowed us to assess the robustness of the integrated system and evaluate its ability to recover the LiDAR-based state estimation using the GPS/INS modality as a reliable fallback. A evaluation video can be found at the following link: ¹.

¹<https://youtu.be/qnaOq1lsJOo>

E. Efficient LiDAR-based state estimator

1) *Efficient registration method*: To enable dense registration using 128-channel or solid-state LiDAR, we encountered a significant CPU bottleneck during the covariance estimation process, particularly while performing the corresponding points search algorithm. To address this limitation and enhance computational efficiency, we successfully utilized CUDA programming, leveraging GPU acceleration for the nearest points search and covariance computation. This approach effectively overcame the performance constraints associated with CPU-based methods.

Furthermore, we conducted an in-depth investigation into the impact of various kernel descriptors on the rotational error within our registration method. To ensure efficient computation, we systematically tested multiple kernel descriptors. Remarkably, our proposed Laplacian method emerged as the most effective, yielding the lowest errors across all evaluation metrics. Detailed results are presented in Table V.

TABLE V
COMPREHENSIVE COMPARISON OF KERNEL DESCRIPTORS

Kernel Descriptor	rmse	mean	median	std
Polynomial	164.93	143.97	125.01	80.47
HI	15.94	14.75	17.19	6.04
Gaussian	23.28	19.70	18.36	12.39
RBF	11.14	9.69	8.14	5.48
Laplacian	10.67	9.24	8.17	5.32

* Leaf size = 1.0 m

2) *Evaluation on Challenging Dataset*: We conducted an evaluation of our efficient LiDAR-inertial-vehicle model odometry on the demanding Monza circuit to assess its performance in handling high lateral acceleration and dynamic rotation at speeds of up to 200 km/h on the road course circuit.

When the inertial and vehicle models are not integrated in dynamic scenarios, our LiDAR-only odometry exhibits significant errors and struggles to cope with environments where similar features are repeated as shown in Fig 10.

To address this limitation, we integrated the LiDAR data with inertial and vehicle motion models, resulting in improved odometry performance and robustness in high-speed and dynamic driving scenarios. Our integrated approach effectively overcomes challenges posed by repeated features and yields more accurate and reliable state estimation, as demonstrated in the Monza circuit evaluation.

A evaluation video can be found at the following link: ².

3) *Comprehensive evaluation with benchmarks*: We conducted a comprehensive evaluation of our efficient LiDAR-based method by comparing it with publicly available LiDAR odometry algorithms. Our proposed cuda-accelerated method, which utilizes a pre-built map, demonstrated superior performance even with significantly lower CPU usage compared to other methods.

While our proposed method may exhibit slightly less accuracy than methods using CPU-based covariance estimation,

²<https://youtu.be/C-H2i3JvJ4>

TABLE VI
COMPARISON WITH THE STATE-OF-THE-ARTS ON ES DATASET.

Method	rmse	mean	median	std	cpu(%)		
					mean	max	min
BLIO	2.745	2.632	2.585	0.779	10.8	23.81	7.73
DLO	6.142	4.775	3.414	3.862	3.22	4.92	2.24
Faster-LIO	3.574	3.138	3.199	1.710	2.94	3.92	2.29
Fast-LIO	3.801	3.319	3.430	1.853	2.45	2.97	2.13
KISS-ICP	29.802	24.655	22.907	16.74	8.28	12.79	5.63
LEGO-LOAM	22.270	20.359	18.099	9.026	-	-	-
Proposed(cpu)	12.45	10.89	9.28	6.04	-	-	-
Proposed(cuda)	25.618	21.064	18.44	14.581	1.17	1.43	1.04
Proposed(cuda)_with_map	1.887	1.579	1.372	1.032	1.65	1.97	1.43
Proposed(cuda)_with_pgo	6.764	5.647	4.859	3.722	3.68	6.53	1.19

*Due to the high computational demands of DLO, KISS-ICP cannot be executed using a leaf size of 1.0m on dense point cloud data. Therefore, all algorithms were evaluated using data downsampled to 2.0m with identical conditions.

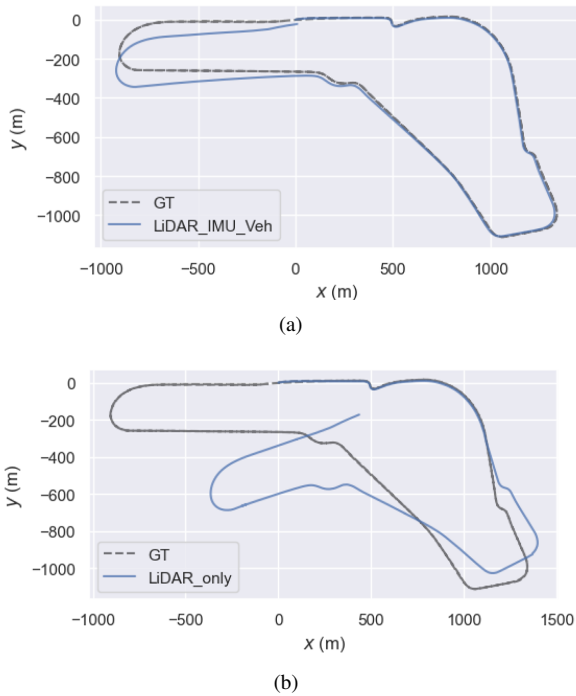


Fig. 10. Comparison of LiDAR odometry with and without IMU and vehicle information integration. (a) LiDAR odometry with preintegrated IMU and vehicle information. (b) LiDAR-only odometry without preintegrated IMU and vehicle information.

this discrepancy can be compensated for through pose graph optimization. Given that our deployment environment is a race track, we found that our loop closing method, which utilizes race track geometry, efficiently identifies re-visited positions and detects loops.

To further illustrate the effectiveness of our approach, we provide benchmark comparisons and present the results of LiDAR odometry evaluation on the Everland Speedway in Figure 11 and Table VI, respectively. The data showcases

the robustness and efficiency of our method in real-world scenarios.

F. Resilient navigation during GPS degradation

This study proposed a resilient navigation system that enables the race car to continue to follow the race track even in the event of a localization failure. We computed wall following path \mathbf{p}_w using Eq. 26 utilizing direct perception information until the completion of localization recover. As shown in Fig. 12(a),12(b), our resilient navigation system came up with critical degradation on all GPS units. In situations of localization failure caused by completely degraded measurement, our resilient navigation algorithm allowed the race car to maintain stability and continue driving away from wall. When analyzing the lateral steering command that follows the racing line based on localization, we found the negative directional steering command causing the vehicle to crash onto the wall, as illustrated in 12(a). More details can be seen online video ³.

G. Resilient navigation under incorrect desired path

During a test run, an incorrect desired path was accidentally given to the system. This happened due to the bias originated from the satellite imagery of the racetrack when the desired path was computed. As shown in Fig. 13(a), the incorrect desired path, also referred to as an abnormal path, could lead dangerously narrow gap to the race wall. When the distance between the wheel and wall became smaller than the emergency threshold as depicted in Fig. 13(b), the resilient navigation system was triggered and provided counter-directional control. Thanks to the resilient navigation system, the wheel to wall distance was successfully maintained bigger than the emergency threshold even though the vehicle kept trying to track the incorrect desired path and approaching to the race wall.

³<https://youtu.be/fiSqdMDmjGo>

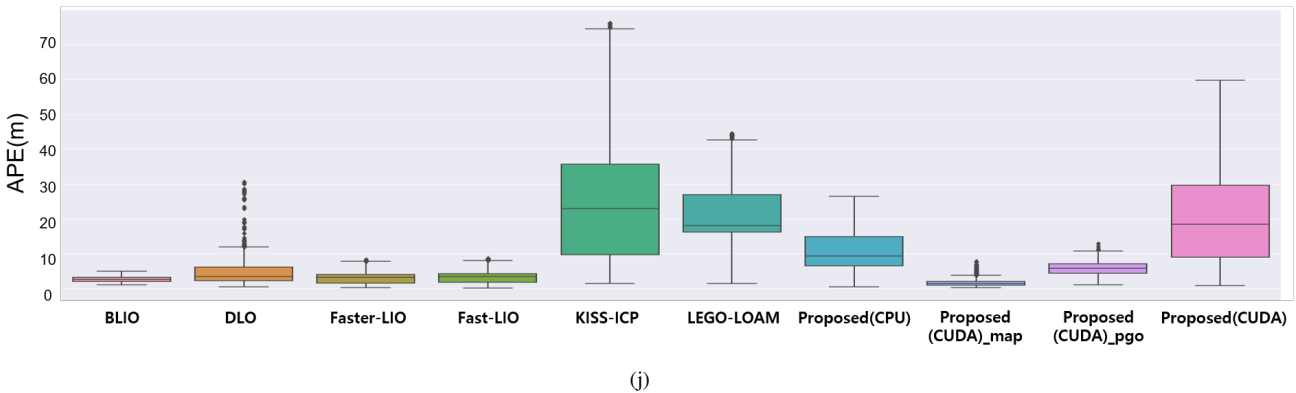
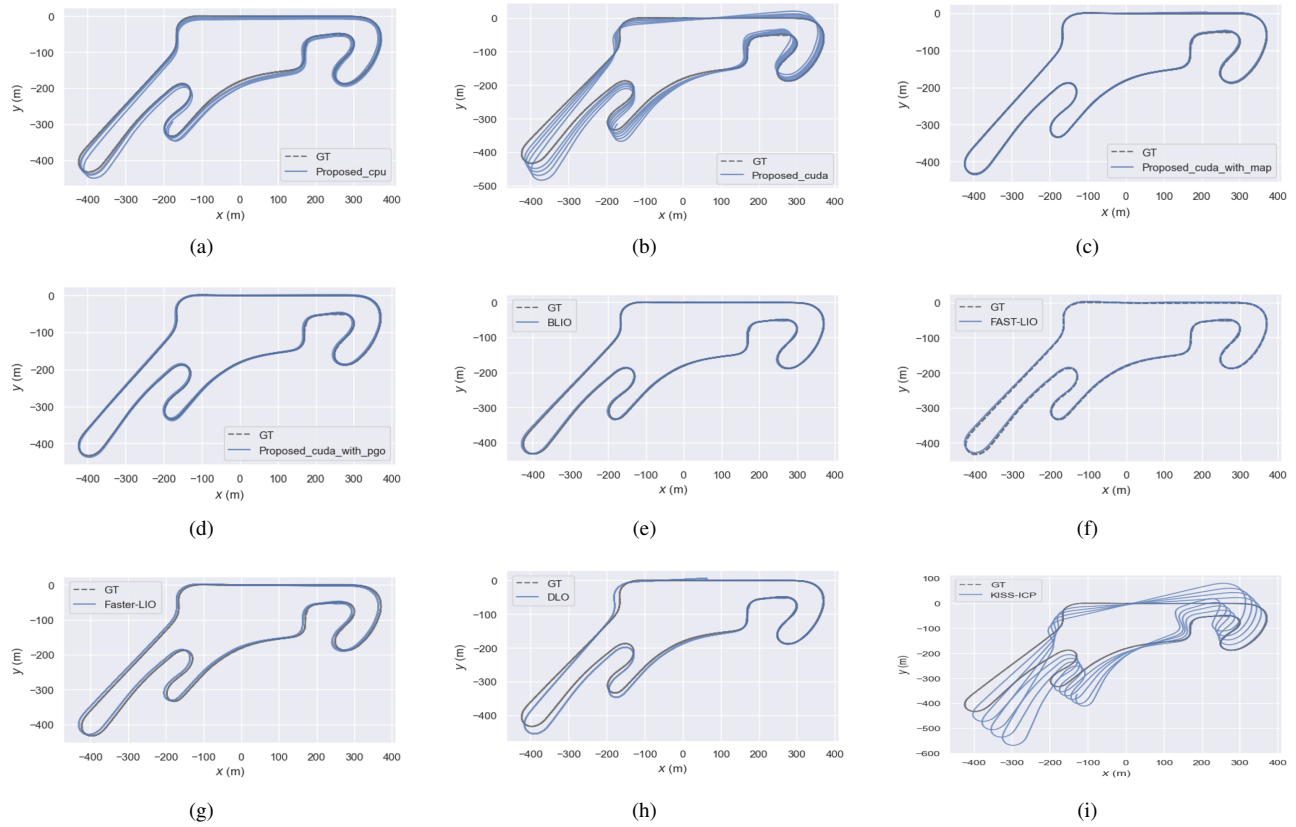


Fig. 11. Comparison of different localization methods (a) V-FAST-GICP, (b) KISS-ICP, (c) GICP, (d) Proposed method. Ground truth is obtained by leveraging GPS signals during the map construction process (e) BLIO, (f) FAST-LIO, (g) Faster-LIO, (h) DLO, (i) KISS-ICP

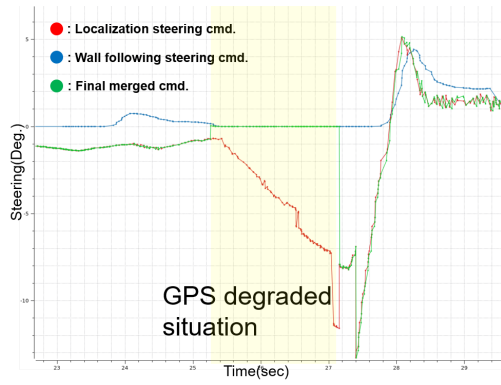
V. CONCLUSION

Our study presents a comprehensive approach to enhance the state estimator for high-speed autonomous race cars, effectively addressing challenges related to unreliable measurements, localization failures, and computing resource management.

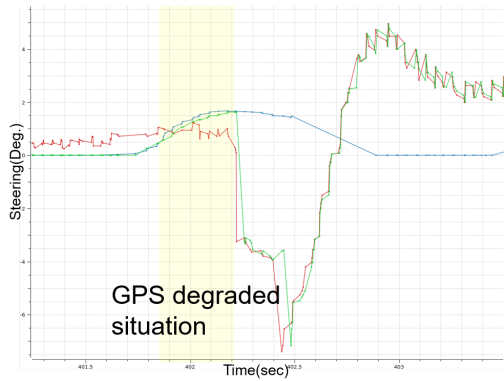
The proposed robust localization system leverages Bayesian-based probabilistic evaluation of multimodal measurements, ensuring the utilization of credible data for precise and reliable localization, even under harsh racing conditions.

To overcome potential localization failures during intense racing, our resilient navigation system enables the race car to continue track-following by utilizing direct perception information in planning and execution, ensuring continuous performance despite localization disruptions.

Efficient computing resource management plays a crucial role in avoiding overload and system failure. We achieve optimized computing resources through an efficient LiDAR-based state estimation method. By harnessing CUDA programming and GPU acceleration, we efficiently perform nearest points search and covariance computation, overcoming CPU bottlenecks.



(a)



(b)

Fig. 12. Proposed resilient navigation system which prevents crashes caused by critical GPS degradation. (a) The proposed algorithm keeps the racing car at a certain distance from the wall for approximately 2 s to prevent crashing. (b) After receiving reasonable measurement data, the final steering command uses the localization-based command.

Our proposed approach is validated through real-world and simulation tests, demonstrating its robust performance and resilience. The system effectively recovers from failures, preventing accidents and ensuring race car safety throughout the driving experience.

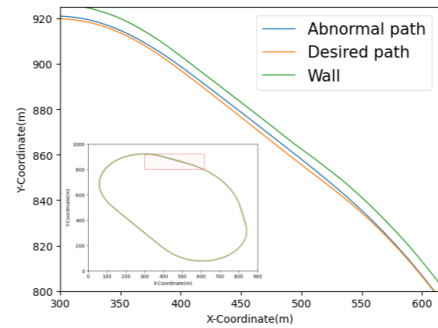
As part of future work, we will continue to explore cutting-edge vision-based methods for drivable area perception as edge computing capabilities evolve and improve, further enriching our state estimation capabilities.

ACKNOWLEDGMENT

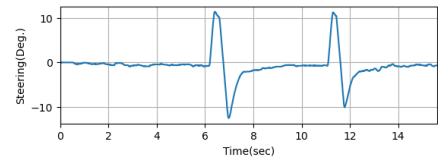
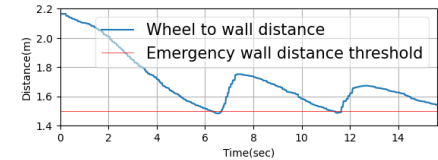
We thank Dr Hoam Chung at Monash University for constructive feedback about the organization of the manuscript.

REFERENCES

- [1] Guang-Zhong Yang, Jim Bellingham, Pierre E Dupont, Peer Fischer, Luciano Floridi, Robert Full, Neil Jacobstein, Vijay Kumar, Marcia McNutt, Robert Merrifield, et al. The grand challenges of science robotics. *Science robotics*, 3(14):eaar7650, 2018.
- [2] Andrey Soloviev. Tight coupling of gps, laser scanner, and inertial measurements for navigation in urban environments. In *2008 IEEE/ION Position, Location and Navigation Symposium*, pages 511–525. IEEE, 2008.



(a)



(b)

Fig. 13. Proposed resilient navigation system prevents abnormal cases from collisions. (a) A magnified representation of the red-shaded region of entire path. An error parameter was present for the track boundary of the abnormal path, causing the wheel to wall distance abnormally small, that can potentially lead to collision with the wall. (b) The subplot below refers to the final merged command. The resilience system is triggered when the distance between the wheel and the wall falls below the established emergency threshold. Positive steering values indicate counter-directional control against the wall.

- [3] Yanbin Gao, Shifei Liu, Mohamed M Atia, and Aboelmagd Noureldin. Ins/gps/lidar integrated navigation system for urban and indoor environments using hybrid scan matching algorithm. *Sensors*, 15(9):23286–23302, 2015.
- [4] Andrey Soloviev, Dustin Bates, and Frank Van Graas. Tight coupling of laser scanner and inertial measurements for a fully autonomous relative navigation solution. *Navigation*, 54(3):189–205, 2007.
- [5] Guowei Wan, Xiaolong Yang, Renlan Cai, Hao Li, Yao Zhou, Hao Wang, and Shiyu Song. Robust and precise vehicle localization based on multi-sensor fusion in diverse city scenes. In *2018 IEEE international conference on robotics and automation (ICRA)*, pages 4670–4677. IEEE, 2018.
- [6] Xiaobin Xu, Lei Zhang, Jian Yang, Chenfei Cao, Wen Wang, Yingying Ran, Zhiying Tan, and Minzhou Luo. A review of multi-sensor fusion slam systems based on 3d lidar. *Remote Sensing*, 14(12):2835, 2022.
- [7] Daegy Lee, Hyunki Seong, Seungil Han, Gyuree Kang, D Hunchul Shim, and Yoonjin Yoon. Design, field evaluation, and traffic analysis of a competitive autonomous driving model in the a congested environment. *arXiv preprint arXiv:2210.17302*, 2022.
- [8] Qingqing Li, Jorge Peña Queralt, Tuan Nguyen Gia, Zhuo Zou, and Tomi Westerlund. Multi-sensor fusion for navigation and mapping in autonomous vehicles: Accurate localization in urban environments. *Unmanned Systems*, 8(03):229–237, 2020.
- [9] Xiaobo Che, Zihui Zhang, Yanjie Sun, Yanqiang Li, and Chao Li. A wall-following navigation method for autonomous driving based on lidar in tunnel scenes. In *2022 IEEE 25th International Conference on Computer Supported Cooperative Work in Design (CSCWD)*, pages 594–598. IEEE, 2022.
- [10] György Csaba, László Somlyai, and Zoltán Vámosy. Mobil robot navigation using 2d lidar. In *2018 IEEE 16th world symposium on*

- applied machine intelligence and informatics (SAMI), pages 000143–000148. IEEE, 2018.
- [11] Kyeong-Jin Joo, Sang-Hyeon Bae, Arpan Ghosh, Hyun-Jin Park, and Tae-Yong Kuc. Wall following navigation algorithm for a disinfecting robot. In *2022 19th International Conference on Ubiquitous Robots (UR)*, pages 343–346. IEEE, 2022.
 - [12] Tianqi Wang and Dong Eui Chang. Improved reinforcement learning through imitation learning pretraining towards image-based autonomous driving. In *2019 19th International Conference on Control, Automation and Systems (ICCAS)*, pages 1306–1310. IEEE, 2019.
 - [13] Marcel Zeilinger, Raphael Hauk, Markus Bader, and Alexander Hofmann. Design of an autonomous race car for the formula student driverless (fsd). In *Oagm & Arw Joint Workshop*, 2017.
 - [14] Juraj Kabzan, Miguel I Valls, Victor JF Reijgwart, Hubertus FC Hendriks, Claas Ehmke, Manish Prajapat, Andreas Bühler, Nikhil Gosala, Mehak Gupta, Ramya Sivanesan, et al. Amz driverless: The full autonomous racing system. *Journal of Field Robotics*, 37(7):1267–1294, 2020.
 - [15] Yunpeng Pan, Ching-An Cheng, Kamil Saigol, Keuntaek Lee, Xinyan Yan, Evangelos A Theodorou, and Byron Boots. Imitation learning for agile autonomous driving. *The International Journal of Robotics Research*, 39(2-3):286–302, 2020.
 - [16] Juraj Kabzan, Lukas Hewing, Alexander Liniger, and Melanie N Zeilinger. Learning-based model predictive control for autonomous racing. *IEEE Robotics and Automation Letters*, 4(4):3363–3370, 2019.
 - [17] Bharathan Balaji, Sunil Mallya, Sahika Genc, Saurabh Gupta, Leo Dirac, Vineet Khare, Gourav Roy, Tao Sun, Yunzhe Tao, Brian Townsend, et al. Deepracer: Educational autonomous racing platform for experimentation with sim2real reinforcement learning. *arXiv preprint arXiv:1911.01562*, 2019.
 - [18] Peter R Wurman, Peter Stone, and Michael Spranger. Challenges and opportunities of applying reinforcement learning to autonomous racing. *IEEE Intelligent Systems*, 37(3):20–23, 2022.
 - [19] Jonathan Francis, Bingqing Chen, Siddha Ganju, Sidharth Kathpal, Jyotish Poonganam, Ayush Shivani, Sahika Genc, Ivan Zhukov, Max Kumskov, Anirudh Koul, et al. Learn-to-race challenge 2022: Benchmarking safe learning and cross-domain generalisation in autonomous racing. *arXiv preprint arXiv:2205.02953*, 2022.
 - [20] Alexander Liniger, Alexander Domahidi, and Manfred Morari. Optimization-based autonomous racing of 1: 43 scale rc cars. *Optimal Control Applications and Methods*, 36(5):628–647, 2015.
 - [21] Varundev Suresh Babu and Madhur Behl. fltenth. dev-an open-source ros based fl/10 autonomous racing simulator. In *2020 IEEE 16th International Conference on Automation Science and Engineering (CASE)*, pages 1614–1620. IEEE, 2020.
 - [22] Johannes Betz, Hongrui Zheng, Alexander Liniger, Ugo Rosolia, Phillip Karle, Madhur Behl, Venkat Krovvi, and Rahul Mangharam. Autonomous vehicles on the edge: A survey on autonomous vehicle racing. *IEEE Open Journal of Intelligent Transportation Systems*, 2022.
 - [23] Johannes Betz, Tobias Betz, Felix Fent, Maximilian Geisslinger, Alexander Heilmeyer, Leonhard Hermansdorfer, Thomas Herrmann, Sebastian Huch, Phillip Karle, Markus Lienkamp, et al. Tum autonomous motorsport: An autonomous racing software for the indy autonomous challenge. *arXiv preprint arXiv:2205.15979*, 2022.
 - [24] Joshua Spisak, Andrew Saba, Nayana Suvarna, Brian Mao, Chuan Tian Zhang, Chris Chang, Sebastian Scherer, and Deva Ramanan. Robust modeling and controls for racing on the edge. *arXiv preprint arXiv:2205.10841*, 2022.
 - [25] Gabriel Hartmann, Zvi Shiller, and Amos Azaria. Competitive driving of autonomous vehicles. *IEEE Access*, 10:111772–111783, 2022.
 - [26] Alexander Heilmeyer, Alexander Wischnewski, Leonhard Hermansdorfer, Johannes Betz, Markus Lienkamp, and Boris Lohmann. Minimum curvature trajectory planning and control for an autonomous race car. *Vehicle System Dynamics*, 2019.
 - [27] Fabian Christ, Alexander Wischnewski, Alexander Heilmeyer, and Boris Lohmann. Time-optimal trajectory planning for a race car considering variable tyre-road friction coefficients. *Vehicle system dynamics*, 59(4):588–612, 2021.
 - [28] Leonhard Hermansdorfer, Johannes Betz, and Markus Lienkamp. A concept for estimation and prediction of the tire-road friction potential for an autonomous racecar. In *2019 IEEE Intelligent Transportation Systems Conference (ITSC)*, pages 1490–1495. IEEE, 2019.
 - [29] Thomas Herrmann, Francesco Passigato, Johannes Betz, and Markus Lienkamp. Minimum race-time planning-strategy for an autonomous electric racecar. In *2020 IEEE 23rd International Conference on Intelligent Transportation Systems (ITSC)*, pages 1–6. IEEE, 2020.
 - [30] Alexander Wischnewski, Thomas Herrmann, Frederik Werner, and Boris Lohmann. A tube-mpc approach to autonomous multi-vehicle racing on high-speed ovals. *IEEE Transactions on Intelligent Vehicles*, 2022.
 - [31] Alexander Wischnewski, Maximilian Geisslinger, Johannes Betz, Tobias Betz, Felix Fent, Alexander Heilmeyer, Leonhard Hermansdorfer, Thomas Herrmann, Sebastian Huch, Phillip Karle, et al. Indy autonomous challenge-autonomous race cars at the handling limits. In *12th International Munich Chassis Symposium 2021*, pages 163–182. Springer, 2022.
 - [32] Chanyoung Jung, Seungwook Lee, Hyunki Seong, Andrea Finazzi, and David Hyunchul Shim. Game-theoretic model predictive control with data-driven identification of vehicle model for head-to-head autonomous racing. *arXiv preprint arXiv:2106.04094*, 2021.
 - [33] Lu Tao, Yousuke Watanabe, Shunya Yamada, and Hiroaki Takada. Comparative evaluation of kalman filters and motion models in vehicular state estimation and path prediction. *The Journal of Navigation*, 74(5):1142–1160, 2021.
 - [34] Adam Charles. Kalman filtering: A bayesian approach, 2017.
 - [35] Roy De Maesschalck, Delphine Jouan-Rimbaud, and Désiré L Massart. The mahalalanobis distance. *Chemometrics and intelligent laboratory systems*, 50(1):1–18, 2000.
 - [36] Frank Dellaert. Factor graphs and gtsam: A hands-on introduction. *Georgia Institute of Technology, Tech. Rep*, 2:4, 2012.
 - [37] Kenji Koide, Masashi Yokozuka, Shuji Oishi, and Atsuhiko Banno. Voxelized gicp for fast and accurate 3d point cloud registration. In *2021 IEEE International Conference on Robotics and Automation (ICRA)*, pages 11054–11059. IEEE, 2021.
 - [38] Daegyu Lee, Gyuree Kang, Boseong Kim, and D Hyunchul Shim. Assistive delivery robot application for real-world postal services. *IEEE Access*, 9:141981–141998, 2021.
 - [39] Xiangfei Qian and Cang Ye. Ncc-ransac: A fast plane extraction method for 3-d range data segmentation. *IEEE transactions on cybernetics*, 44(12):2771–2783, 2014.
 - [40] Lin Li, Fan Yang, Haihong Zhu, Dalin Li, You Li, and Lei Tang. An improved ransac for 3d point cloud plane segmentation based on normal distribution transformation cells. *Remote Sensing*, 9(5):433, 2017.
 - [41] Shruti Karbhari and Shadi Alawneh. Gpu-based parallel implementation of k-means clustering algorithm for image segmentation. In *2018 IEEE International Conference on Electro/Information Technology (EIT)*, pages 0052–0057. IEEE, 2018.
 - [42] Anh Nguyen, Abraham Monrroy Cano, Masato Edahiro, and Shinpei Kato. Fast euclidean cluster extraction using gpus. *Journal of Robotics and Mechatronics*, 32(3):548–560, 2020.
 - [43] Radu Bogdan Rusu. Semantic 3d object maps for everyday manipulation in human living environments. *KI-Künstliche Intelligenz*, 24(4):345–348, 2010.
 - [44] Hyunki Seong, Chanyoung Chung, and David Hyunchul Shim. Data-driven model identification via hyperparameter optimization for the autonomous racing system. *arXiv preprint arXiv:2301.01470*, 2023.